Radar Imaging System for In-Service Wind Turbine Blades Inspections: Initial Results from a Field Installation at a 2 MW Wind Turbine

**Jochen Moll[1, *], Jonas Simon[1], Moritz Mälzer[1],
Viktor Krozer[1], Dimitry Pozdniakov[2], Rahmi Salman[2],
Manfred Dürr[3], Michael Feulner[4], Andreas Nuber[4], and Herbert Friedmann[4]**

Abstract—This paper presents an imaging radar system for structural health monitoring (SHM) of wind turbine blades. The imaging radar system developed here is based on two frequency modulated continuous wave (FMCW) radar sensors with a high output power of 30 dBm. They have been developed for the frequency bands of 24,05 GHz–24,25 GHz and 33.4 GHz–36.0 GHz, respectively. Following the successful proof of damage detection and localization in laboratory conditions, we present here the installation of the sensor system at the tower of a 2 MW wind energy plant at 95 m above ground. The realization of the SHM-system will be introduced including the sensor system, the data acquisition framework and the signal processing procedures. We have achieved an imaging of the rotor blades using inverse synthetic aperture radar techniques under changing environmental and operational condition. On top of that, it was demonstrated that the front wall and back wall radar echo can be extracted from the measured signals demonstrating the full penetration of wind turbine blades during operation.

1. INTRODUCTION

Condition monitoring (CM) and structural health monitoring (SHM) systems are important for reducing the maintenance and operational costs of wind energy plants [1–3]. Especially, the blades of a wind turbine are critical structural components, because of their large dimensions as well as their diverse failure mechanisms [4–7]. Among the various monitoring techniques vibration-based approaches as well as methods based on acoustic emission are widely used to assess the health status of a wind turbine blade. However, both techniques have drawbacks either in terms of their damage detection sensitivity or a limited monitoring area.

In recent years, radar methods in the microwave, millimeter-wave and Terahertz frequency range have been investigated intensively for the non-destructive inspection of fiber composite materials [8, 9]. A structural damage, such as a delamination, can be detected based on a local change in the electromagnetic properties [2]. In contrast to related techniques the electromagnetic NDT methods are non-contact, enable a one-sided scanning, are free of couplants and without safety concerns due to the low radiated power [10]. Electromagnetic waves are able to penetrate non-conductive materials and also provide the material's spectral response [11]. Depending on the frequency band chosen for the radar, the probing wavelength is relatively short, which results in a relatively good spatial resolution.

These interesting features show the great potential of electromagnetic waves in the microwave and millimeter-wave (mm-wave) regime in future CM- and SHM-systems.

Only a few examples are reported in the literature which specifically deal with the non-destructive testing of wind turbine blades using high frequency methods. Li et al. [10] study glass fiber T-joints as part of wind turbine blades using an open-ended waveguide sensor in the frequency range from 18–26 GHz. They were able to detect a delamination width of 0.2 mm when the sensor is close to the surface of the structure. A microwave interferometric technique at 24 GHz is used in [12] for volumetric inspection of wind turbine blades. Recently, a real-time millimeter wave imaging system for NDT applications at 30 GHz has been proposed in [13]. A wind turbine trailing edge was studied in [14] in the frequency range from 0.1 to 1 THz. The considered sample contained several layers of glass fiber composite, balsa wood, and adhesive. Finally, a recent review on short-range microwave radar systems reports on several examples of measuring the dynamic response of the structure based on the Doppler effect [15]. Changes in the dynamic properties of the structure, such as a wind turbine blade, can be attributed to a structural damage.

The following conclusions can be drawn from this literature overview:

(i) Damage detection sensitivity: Microwave and mm-wave electromagnetic methods have interesting damage detection capabilities. Several damage types have been successfully identified in glass fiber composite structures that are widely used in wind turbine blades including delaminations, debonding, impact damage etc..

(ii) Optimal frequency band: Several frequency bands up to 1 THz have been investigated. Although higher frequencies promise a better damage reconstruction and a higher sensitivity towards smaller defects, the waves attenuation increases strongly and limits practical applicability. Hence, frequencies in the higher microwave and lower millimeter-wave frequency range are of high interest for practical monitoring applications due to a good material penetration, little atmospheric losses and a relatively short wavelength.

(iii) Laboratory systems: Most of the high frequency systems have measured samples in the laboratory environment. A field installation of a microwave and mm-wave radar system for a continuous structural analysis has not been demonstrated yet.

This paper continues the recent work by the authors on radar-based SHM of wind turbine blades [16, 17]. In the previous publications we showed a promising damage detection and localization performance in a glass fiber composite plate and a rotor blade tip sample. That analysis has been performed in the laboratory environment where no variations in environmental and operational conditions occur. Moreover, we were able to show that a full penetration of the rotor blade is possible in this frequency band [18].

The novelty of the present paper is to show a radar system installation at the tower of an operational 2 MW wind energy plant at 95 m above ground. Structural inspection takes place when the blade passes the radar sensor at 6 o'clock position. Besides the two FMCW radar systems, we will describe the data acquisition procedure and signal processing techniques. The analysis includes a data-driven method to identify the blade passage under different environmental and operational conditions. On top of that, imaging results of the rotor blades are presented using inverse synthetic aperture radar techniques, such as ω-k-algorithm and range migration algorithm.

2. DESCRIPTION OF THE RADAR MEASUREMENT SYSTEM

2.1. Radar Subsystem

The measurement system in this paper consists of two independent frequency-modulated continuous wave (FMCW) radar sensors operating in the frequency bands from 24.05 GHz–24.25 GHz and 33.4 GHz–36.0 GHz, respectively. The radar sensors are placed in a weatherproof radome and are installed at the tower of a 2 MW wind energy plant (WEP) approximately 95 m above ground. Both radars transmit simultaneously electromagnetic radiation towards the rotor blades. Exploiting the rotation of the rotor blades it is possible to perform a health monitoring of certain regions of the wind turbine blade with a fixed sensor system. A photo of the sensor system and its installation at the tower of a wind turbine can be seen in Fig. 1. Further system details are provided in the overview depicted in Fig. 2.

(a)   (b)
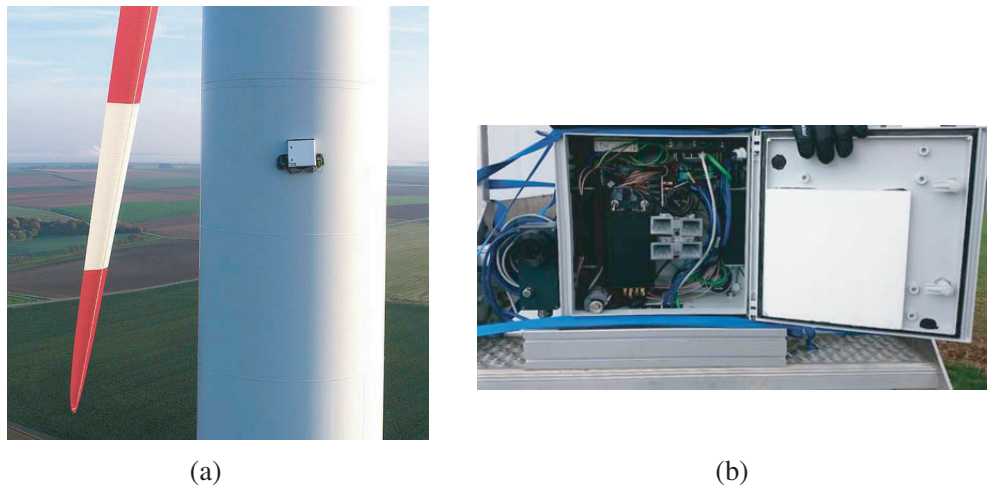
Figure 1. (a) Sensor unit installation at a 2 MW wind energy plant at 95 m above ground. (b) Photo of the sensor system.
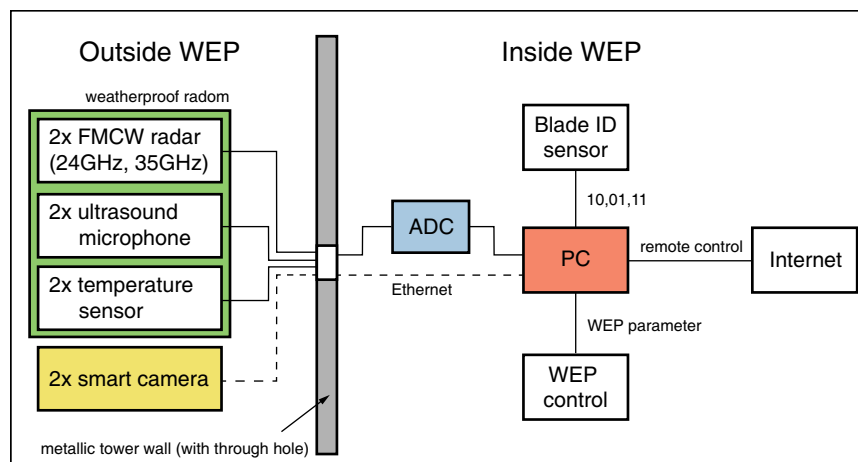
Figure 2. System overview with the sensors outside the wind energy plant (WEP) and components inside the WEP tower, after [19]. Ultrasound microphones and smart cameras are used for acoustic and visual detection of bats, cf. [20], and will not be further considered in this article.

Each of the two radar systems provides a high output power of about 30 dBm which enables a complete penetration of the composite fiber blades [21]. The sweep time of the 35 GHz radar sensor is 500 µs, and the one for the 24 GHz system is 100 µs. This means that the sweep time for the 35 GHz system is five times longer than the 24 GHz system. Each bistatic radar system consists of two broadband horn antennas, and each has an antenna gain of approximately 24 dBi. The antennas are arranged symmetrically to each other so that the measurements from both systems can be compared easily. The output of both radar systems is an in-phase signal (I-signal), a quadrature signal (Q-signal) and a trigger signal. The trigger signal is used to extract the relevant signal components corresponding to the frequency sweep as demonstrated in [16]. The I- and Q-signals are further processed to compute the radar signals (so called range profiles) by means of an inverse Fourier Transform. These signals are the basis for in-service radar imaging of the wind turbine blades.

For completeness, the monitoring system also includes two ultrasound microphones and two smart cameras, in conjunction with the radar, for acoustic and visual detection of bats for a bat-friendly wind turbine operation [20, 22].
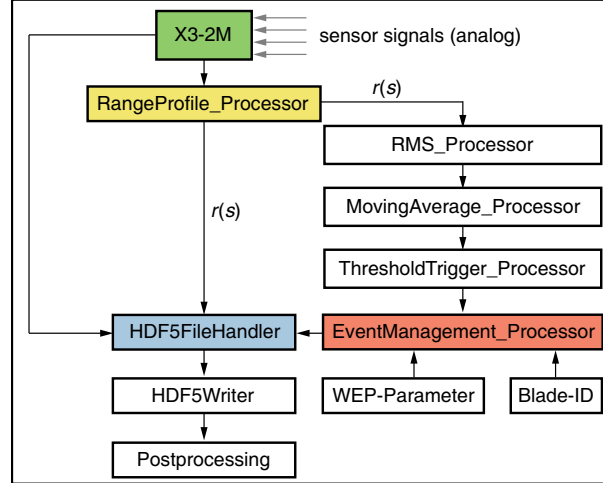
Figure 3. Schematic to illustrate the real-time data acquisition and signal preprocessing workflow. The analog sensor signals include the raw sigals from both radar systems (I-signal, Q-signal and trigger signal) as well as the temperature and microphone signals. The processors describe the workflow of the radar signals from pre- to post-processing.

2.2. Data Acquisition and Data-Driven Blade Detection

The analog signals from the sensor modules are forwarded to a multichannel A/D-converter X3-2M from Innovative Integration (Camarillo, USA) as shown in Fig. 3. This device enables continuous streaming of measurement data to the PC at a high sampling rate of 5 MSPS. By means of simultaneous sampling, a synchronization of the sensor signals can be achieved. The raw data coming from both radar systems, i.e., I-signal, Q-signal and trigger-signal, are processed by the *RangeProfile_Processor*. In this processor, the raw data are segmented based on the trigger information. Next, a complex inverse Fourier transform leads to the range profile $r(s)$ [23]. The range profiles are forwarded to the *RMS_Processor* in which the root-mean-square (RMS) of the range profile $r(s)$ is computed in the following way:

$$Y^{RMS} = \sqrt{\frac{1}{S_{\max} - S_{\min}} \int_{S_{\min}}^{S_{\max}} r^2(s) ds} \tag{1}$$

In this equation, $S_{\min}$ is the minimum and $S_{\max}$ the maximum distance of interest. We define $S_{\min} = 0\,\mathrm{m}$ and $S_{\max} = 15\,\mathrm{m}$, because the distance between the tower and the blade is approximately $10\,\mathrm{m}$. Further increasing $S_{\max}$ would unnecessarily decrease signal-to-noise ratio (SNR). The RMS-metric is central in the identification of a blade passage, because it increases when the blade is in the radar beam, and constant in all other cases.

It was found experimentally that the RMS-value is fluctuating which makes a reliable detection of the rotor blades difficult. Based on this observation we have implemented a real-time moving average filter in the *MovingAverage_Processor* for smoothing the RMS-curves:

$$\bar{Y}_j^{RMS} = \frac{1}{n} \sum_{k=j}^{j+n-1} Y_k^{RMS} \tag{2}$$

In this equation, the filter order of the moving average is $n = 21$.

Since we are only interested in the signals that correspond to the blade passage, it is possible to ignore all signals between two subsequent blade passages. As soon as a threshold is exceeded we reliably identify the signal increase that corresponds to a blade passage. This functionality is implemented in the *ThresholdTrigger_Processor*. Here, we define the threshold τ_i at the discrete time instance i based on the statistical properties of the measured signals using its moving average $\bar{Y}^{RMS}$ and its moving standard deviation $\bar{\sigma}$:

$$\tau_i = \bar{Y}_i^{RMS} + \eta \cdot \bar{\sigma}. \tag{3}$$

In this equation, we introduce the weighting factor η that is empirically defined as $\eta = 1.3$. The moving average and moving standard deviation are implemented in such a way that both quantities are updated in real-time as soon as a new RMS value has been computed. The updating is important, because otherwise it is not possible to follow a certain trend in the data that is induced by changing environmental and operational conditions, such as rain. The computation takes into account a total of 10,001 measurements per radar receiver channel which corresponds to a time period of approximately 5.2 seconds. This means that although the number of measurements is high, the corresponding measurement period is relatively short.

The *EventManagement_Processor* evaluates if a threshold crossing occurs. If this is true, then the current parameters of the wind turbine (wind speed, electrical power etc.) and the corresponding blade-ID (1, 2 or 3) are forwarded with the current signals to the *HDF5FileHandler* that saves the data on hard disc via *HDF5Writer* for the subsequent post processing. In the future, we plan to implement an online methodology so that writing of raw data to the hard disc is not required anymore.

2.3. Image Reconstruction Techniques

Within the last decades, different beamforming techniques have been developed and applied in order to detect, locate and estimate a target, its contour and orientation from the radar data gathered over a 2D aperture. Within this paper, the radar images of the rotor blades are performed with the ω-k algorithm as well as the range migration method. The basic computational difference of both algorithms consists in different domain calculations. Range migration requires a coherent synthetic aperture processing in a summation manner in the time domain whereas the ω-k algorithm performs the backprojection in the frequency-wavenumber domain. Both image reconstruction techniques are well known in the radar community for diverse scenarios, distances and configurations. This is the reason why a detailed description of both algorithms is not provided here. For further information, interested readers may refer to existing literature, e.g., [24–27].
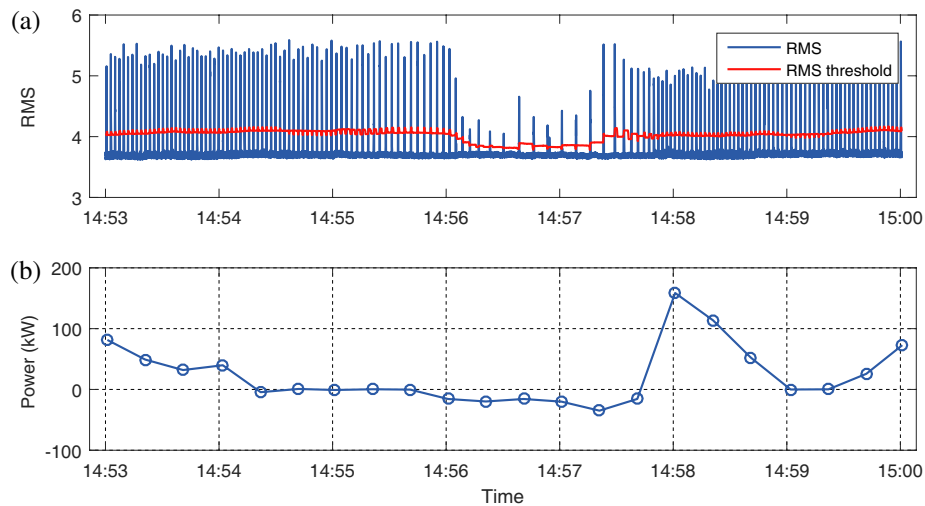
Figure 4. (a) RMS curve based on the 35 GHz radar and corresponding detection threshold over a period of seven minutes; (b) electrical power generated by the wind turbine at the same time. A deceleration of the wind turbine can be observed at negative power levels (standby power of the WEP), and also an acceleration when the electrical power generation increases.
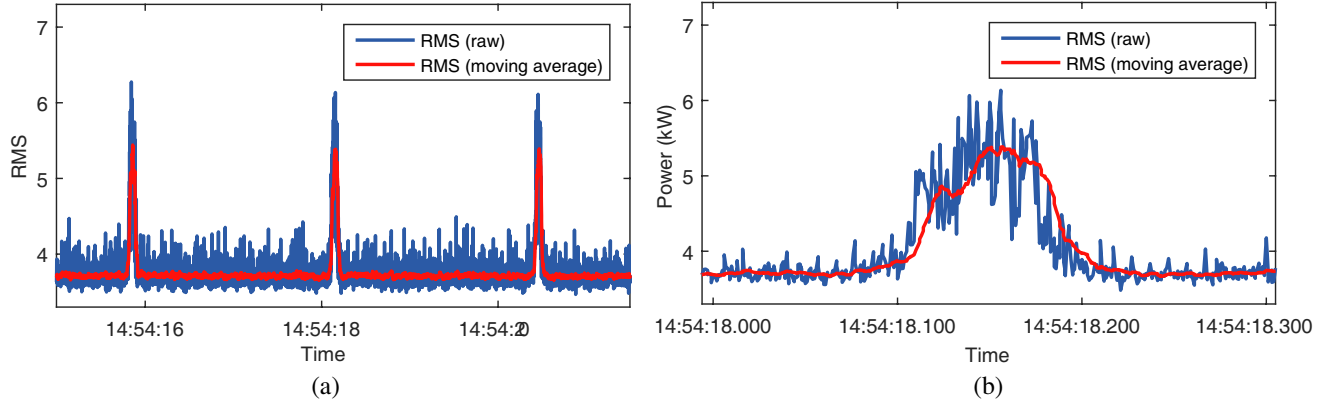
Figure 5. (a) Comparison of the raw RMS curve and the RMS smoothed with the moving average filter for three subsequent blade passages, (b) detailed comparison of a single blade passage.

3. RESULTS

3.1. Identification of a Blade Passage

The top part of Fig. 4 shows the RMS curve and the curve for the threshold over a time period of seven minutes. The bottom part of the same figure depicts the corresponding power of the wind turbine. It is interesting to see that the RMS curve follows a regular pattern. Each peak of the curve corresponds to one blade passage. After three minutes the amplitude of the RMS curves as well as its repetition frequency changes, mainly because the WEP operates in coasting mode. It is worth noting that the threshold curve follows the global trend and always intersects the RMS curve at the expected position. This example shows the importance of continuously updating the threshold limit.

A more detailed analysis of the RMS curve is shown in Fig. 5 which illustrates a comparison between the noisy original RMS curve and its smoothed version. Considering the raw RMS curve an automatic triggering of the measurements is very complicated. Computing the moving average filter online and in real-time reduces the complexity of the blade identification significantly. It should be highlight here, that a robust identification of the blade passage is crucial for the proposed SHM methodology, because only those signals corresponding to a peak in the RMS curve should be analysed for damage assessment. The remaining signals between two blade passages are not relevant for diagnostic purposes and may be discarded.

We have also studied the time period of the peaks in the RMS-curve in Fig. 6. Two examples are considered here, where the turbine generates electrical power of 181 kW and 1,233 kW, respectively. The different time periods can be explained by a different speed of rotation and the corresponding time differences of the rotor blade in the radar beam. In the first case, the blade is illuminated by the radar for 0.1575 s whereas the time period reduces to 0.0824 s in the latter case.

3.2. 2D Radar Imaging

The starting point for the subsequent radar imaging are the range profiles measured with the 35 GHz and 24 GHz radar system. Fig. 8 shows a waterfall diagram, also called radargram, where the 35 GHz signals are shown in Fig. 8(a) and the 24 GHz signals are shown in Fig. 8(b). It can be clearly observed that certain fluctuations occur in the signals originating from the complex scattering of the electromagnetic waves in the rotor blade. Doppler effects due to mechanical vibrations of the radar system or the rotor blade can be ignored due to the sub-second time scale. This also means that vibration-based SHM techniques exploiting Doppler are not feasible in the proposed system concept when the turbine is rotating. It is interesting to see in Fig. 8(c) that the front wall echo can be distinguished from the back wall echo with the 35 GHz radar. On the other hand, the 24 GHz system is not able to resolve the front wall and back wall echo. This result demonstrates that the whole blade, as a multi-material system, can be penetrated and inspected by means of electromagnetic radiation in the mm-wave frequency range.
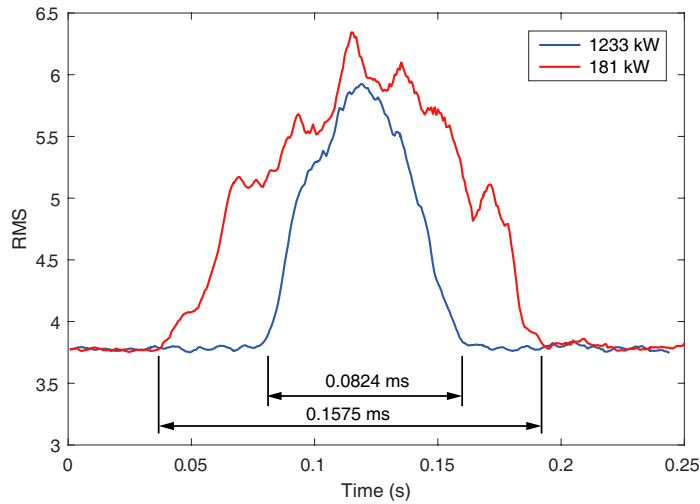
Figure 6. Depending on the current power of the wind energy plant the speed of rotation is different. This leads to the observation that the time of the rotor blade in the radar beam is different and depends on the speed of the rotor blades.
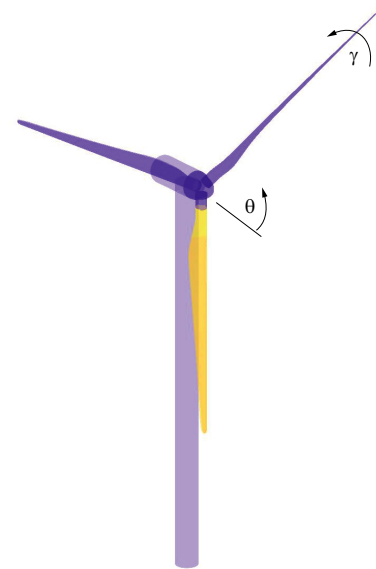

Figure 7. Illustration of the azimuth angle θ and pitch angle γ.
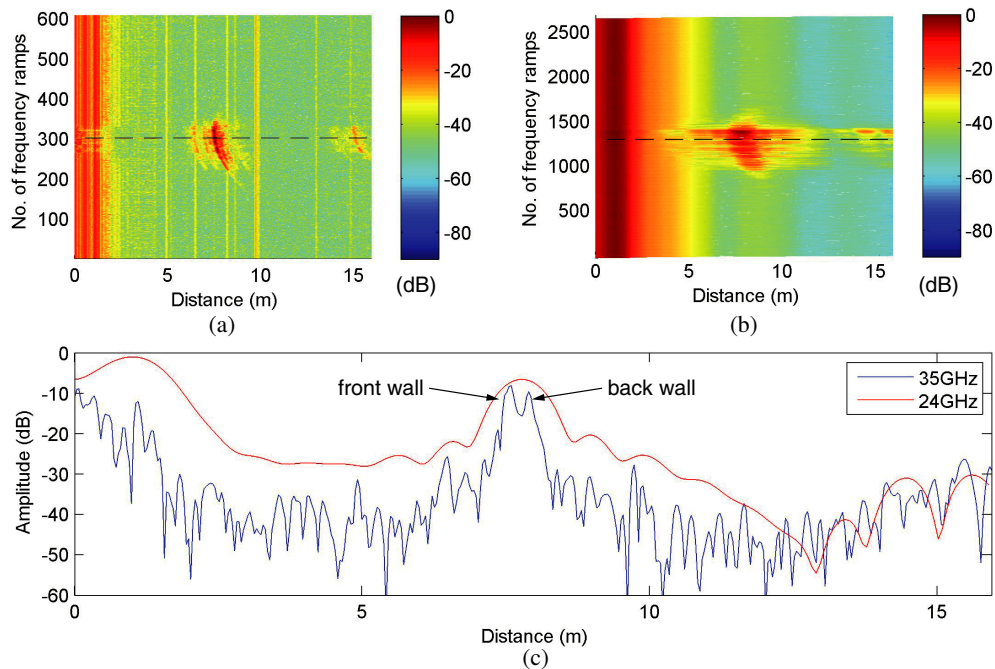

Figure 8. (a) Radargram of the 35 GHz radar system; (b) radargram of the 24 GHz system; (c) Exemplary range profiles showing the front and back wall echo in the 35 GHz signal. Due to the smaller bandwidth and thus reduced range resolution the front and back wall cannot be distinguished in the range profile of the 24 GHz radar system.

Figures 9 and 10 show image reconstruction results for both radar systems and the two image reconstruction techniques introduced above. The underlying radar signals (energy signals) were measured at different parameters of the wind energy plant. In the first case, shown in Fig. 9, the
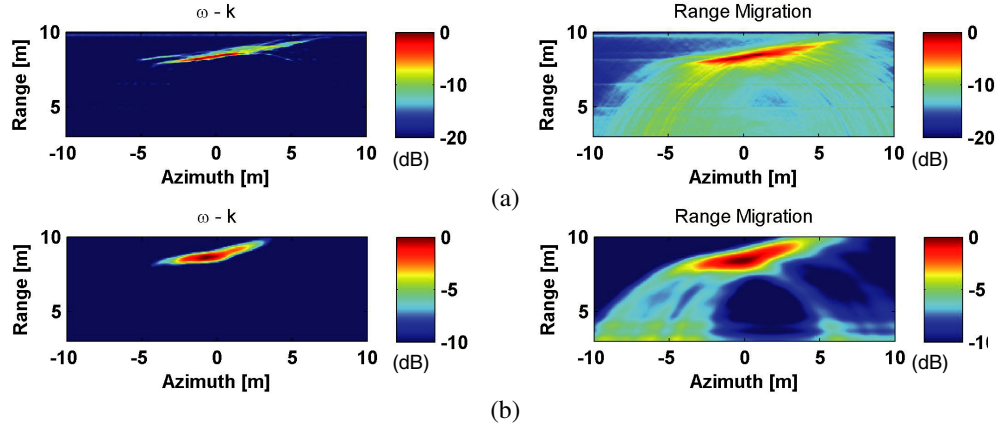
Figure 9. Comparison of 2D imaging of a wind turbine blade: Results for the 35 GHz are presented in (a) and for 24 GHz in (b). The parameters of the wind turbine are: power: 90 kW, azimuth: 182.1° and pitch angle: −0.6°.
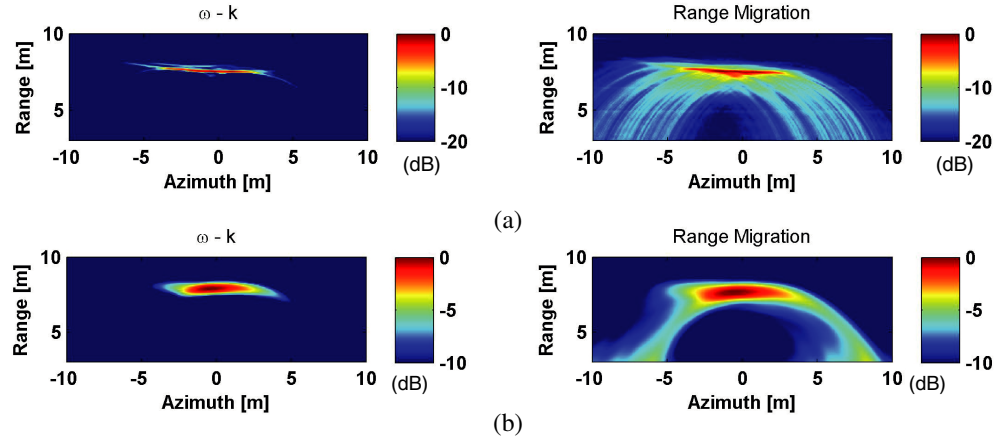
Figure 10. Comparison of 2D imaging of a wind turbine blade: Results for the 35 GHz are presented in (a) and for 24 GHz in (b). The parameters of the wind turbine are: power: 2,000 kW, azimuth: 218.6° and pitch angle: 14.1°.

power of the wind turbine was 90 kW, the azimuth angle was 182.1° and the pitch angle was -0.6°. In the second example, the power of the wind turbine was 2,000 kW, the azimuth angle was 218.6° and the pitch angle was 14.1°. An illustration of the azimuth angle θ and pitch angle γ is shown in Fig. 7.

It can be observed in Fig. 9 and Fig. 10 that both radar systems are able image the rotor blade using ω-k-algorithm and the range migration technique. The former shows a better signal-to-clutter ratio and is thus the preferred image reconstruction technique. Moreover, it can be observed that the position of the blade is reconstructed closer to the tower of the wind turbine when a higher electrical power is generated due to a stronger bending of the blades in response to higher wind forces. Secondly, the radar sensor is installed at an azimuth angle of approximately 220°. The reconstruction of the rotor blade in Fig. 10 is thus aligned horizontally, and the reconstruction of the rotor blade in Fig. 9 is slightly inclined. On one hand, this result is expected, due to the relative orientation of the blade with respect to the radar sensor. On the other hand, this result shows that a radar-based SHM system for rotor blades of wind turbine structures has to deal with changing operational conditions (here: primarily the azimuth angle). Hence, multiple baseline measurements for significant environmental and operational conditions are needed so that damage-related changes in the rotor blade become detectable.

4. CONCLUSIONS

This paper demonstrates that FMCW radar systems in the frequency range from 24.05 GHz–24,25 GHz and 33.4 GHz–36.0 GHz are able to monitor wind turbine blades in real-time. We successfully showed the installation of an imaging radar system at 95 m above ground, in conjunction with the data acquisition infrastructure and the signal processing techniques. The latter included the automatic detection of the blade passage as an important preprocessing step to extract those radar signals that should be used for diagnostic purposes. Next, those signals are processed to compute radar images of wind turbine blades at variable environmental and operational conditions.

Future work will consider a more complex radar system with one transmitter and nine receivers as shown in [28]. Moreover, we have to prove that actual damages, in particular delaminations, but also cracks and detachment of kissing bonds, can be detected during operation of the wind turbine.

REFERENCES

1. Márquez, F. P. G., J. M. P. Pérez, A. P. Marugán, and M. Papaelias, "Identification of critical components of wind turbines using FTA over the time," *Renewable Energy*, Vol. 87, 869–883, March 2016.
2. Yang, R., Y. He, and H. Zhang, "Progress and trends in nondestructive testing and evaluation for wind turbine composite blade," *Renewable and Sustainable Energy Reviews*, Vol. 60, 1225–1250, July 2016.
3. Ciang, C. C., J.-R. Lee, and H.-J. Bang, "Structural health monitoring for a wind turbine system: A review of damage detection methods," *Measurement Science and Technology*, Vol. 19, No. 12, 122001, December 2008.
4. Adams, D., J. White, M. Rumsey, and C. Farrar, "Structural health monitoring of wind turbines: method and application to a HAWT," *Wind Energy*, Vol. 14, No. 4, 603–623, May 2011.
5. Lu, B., Y. Li, X. Wu, and Z. Yang, "A review of recent advances in wind turbine condition monitoring and fault diagnosis," 1–7, 2009.
6. Qiao, W. and D. Lu, "A survey on wind turbine condition monitoring and fault diagnosis — Part I: Components and subsystems," *IEEE Transactions on Industrial Electronics*, Vol. 62, No. 10, 6536–6545, October 2015.
7. Zhou, H. F., H. Y. Dou, L. Z. Qin, Y. Chen, Y. Q. Ni, and J. M. Ko, "A review of full-scale structural testing of wind turbine blades," *Renewable and Sustainable Energy Reviews*, Vol. 33, 177–187, May 2014.
8. Kharkovsky, S. and R. Zoughi, "Microwave and millimeter wave nondestructive testing and evaluation — Overview and recent advances," *IEEE Instrumentation & Measurement Magazine*, Vol. 10, No. 2, 26–38, April 2007.
9. Zhu, Y.-K., G.-Y. Tian, R.-S. Lu, and H. Zhang, "A review of optical NDT technologies," *Sensors*, Vol. 11, No. 12, 7773–7798, August 2011.
10. Li, Z., A. Haigh, C. Soutis, A. Gibson, and R. Sloan, "Microwaves sensor for wind turbine blade inspection," *Applied Composite Materials*, November 2016.
11. Fukasawa, R., "Terahertz imaging: Widespread industrial application in non-destructive inspection and chemical analysis," *IEEE Transactions on Terahertz Science and Technology*, Vol. 5, No. 6, 1121–1127, 2015.

12. Wetzel, K., K. Lee, A. Tran, B. Stakenborghs, and R. J. Woodward, "Volumetric inspection of wind turbine blades using a microwave interferometric technique," *Materials Evaluation*, 477–484, 2016.

13. Ghasr, M. T., M. J. Horst, M. R. Dvorsky, and R. Zoughi, "Wideband microwave camera for real-time 3-D imaging," *IEEE Transactions on Antennas and Propagation*, Vol. 65, No. 1, 258–268, January 2017.

14. Hsu, D. K., K.-S. Lee, J.-W. Park, Y.-D. Woo, and K.-H. Im, "NDE inspection of terahertz waves in wind turbine composites," *International Journal of Precision Engineering and Manufacturing*, Vol. 13, No. 7, 1183–1189, July 2012.

15. Li, C., Z. Peng, T.-Y. Huang, T. Fan, F.-K. Wang, T.-S. Horng, J.-M. Munoz-Ferreras, R. Gomez-Garcia, L. Ran, and J. Lin, "A review on recent progress of portable short-range noncontact microwave radar systems," *IEEE Transactions on Microwave Theory and Techniques*, 1–15, 2017.

16. Moll, J., P. Arnold, M. Mälzer, V. Krozer, D. Pozdniakov, R. Salman, S. Rediske, M. Scholz, H. Friedmann, and A. Nuber, "Radar-based structural health monitoring of wind turbine blades: The case of damage detection," *Structural Health Monitoring: An International Journal*, 147592171772144, August 2017.

17. Arnold, P., J. Moll, M. Mälzer, V. Krozer, D. Pozdniakov, R. Salman, S. Rediske, M. Scholz, H. Friedmann, and A. Nuber, "Radar-based structural health monitoring of wind turbine blades: The case of damage localization," *Wind Energy*, January 2018.

18. Moll, J., V. Krozer, P. Arnold, M. Dürr, R. Zimmermann, R. Salman, D. Hübsch, H. Friedmann, A. Nuber, M. Scholz, and P. Kraemer, "Radar-based structural health monitoring of wind turbine blades," *19th World Conference on Non-Destructive Testing*, 1–8, Munich, Germany, 2016.

19. Moll, J., M. Mälzer, J. Simon, V. Krozer, M. Feulner, H. Friedmann, A. Nuber, R. Salman, D. Pozdniakov, and M. Dürr, "Field demonstration of radar-based SHM of wind turbine blades at a 2 MW wind turbine: Installation, data acquisition and signal analysis," *11th International Workshop on Structural Health Monitoring*, 1–8, Stanford, USA, 2017.

20. Scholz, N., J. Moll, M. Mälzer, K. Nagovitsyn, and V. Krozer, "Random bounce algorithm: real-time image processing for the detection of bats and birds: Algorithm description with application examples from a laboratory flight tunnel and a field test at an onshore wind energy plant," *Signal, Image and Video Processing*, Vol. 10, No. 8, 1449–1456, November 2016.

21. Moll, J. and V. Krozer, "Radar-based mechanical vibration sensing for structural health monitoring applications: A comparison of radar transceiver measurements at 24 GHz and 100 GHz," *8th European Workshop on Structural Health Monitoring*, 1–6, 2016.

22. Moll, J., M. Mälzer, V. Krozer, D. Pozdniakov, R. Salman, J. M. Beetz, and M. Kössl, "Activity monitoring of bats in a laboratory flight tunnel using a 24 GHz FMCW radar system," *11th European Conference on Antennas and Propagation*, 2541–2545, Paris, France, 2017.

23. Soumekh, M., *Synthetic Aperture Radar Signal Processing with MATLAB Algorithms*, Wiley, New York, OCLC: 833493976, 1999.

24. Sakamoto, T., T. Sato, P. Aubry, and A. Yarovoy, "Frequency-domain Kirchhoff migration for near-field radar imaging," 1–4, 2015.

25. Sakamoto, T., T. Sato, P. J. Aubry, and A. G. Yarovoy, "Ultra-wideband radar imaging using a hybrid of kirchhoff migration and stolt F-K migration with an inverse boundary scattering transform," *IEEE Transactions on Antennas and Propagation*, Vol. 63, No. 8, 3502–3512, 2015.

26. Zhuge, X. and A. G. Yarovoy, "Three-dimensional near-field MIMO array imaging using range migration techniques," *IEEE Transactions on Image Processing*, Vol. 21, No. 6, 3026–3033, 2012.

27. Gorham, L. A. and L. J. Moore, "SAR image formation toolbox for MATLAB," 769906–769906-13, April 2010.

28. Arnold, P., J. Moll, and V. Krozer, "Design of a sparse antenna array for radar-based structural health monitoring of wind turbine blades," *IET Radar, Sonar & Navigation*, Vol. 11, No. 8, 1259–1265, August 2017.